Top Curr Chem (2007) 270: 127–153
DOI 10.1007/128_075

Inorganic-Organic Interfacial Interactions in Hydroxyapatite Mineralization Processes

Kimiyasu Sato

National Institute of Advanced Industrial Science and Technology (AIST),
Anagahora 2266-98, Shimoshidami, Moriyama-ku, 463-8560 Nagoya, Japan
sato.kimiyasu@aist.go.jp

Abstract Details of our recent attempts to clarify the self-organization mechanism of hydroxyapatite (HAp) mineralization in natural bodies are presented in this work. In biomineralization processes, inorganic crystals precipitate onto organic matrix surfaces. Organic molecules assembled to monolayer films were employed to reproduce the organic matrices in natural bodies, and the HAp mineralization process onto the organic monolayers were subjected to spectroscopic and structural analytical approaches. Knowledge of interfacial atomic structures is also essential for interpretation of the inorganic-organic interface. We determined the most stable atomic arrangement of the HAp {100} facet using high-resolution transmission electron microscopy. A mechanism of HAp mineralization proposed in view of the experimental results is the highlight of this work.

Keywords Electron microscopy · Hydroxyapatite · Interfacial interactions · IR spectroscopy · Organic matrices

Abbreviations

DF	defocus
FT-IR	Fourier transform IR
HAp	hydroxyapatite
HRTEM	high-resolution transmission electron microscopy
LB	Langmuir–Blodgett
OCP	octacalcium phosphate
SAED	selected area electron diffraction
SAM	self-assembled monolayer

SBF	simulated body fluid
SEM	scanning electron microscopy
TEM	transmission electron microscopy
TF-XRD	thin-film X-ray diffraction
XRD	X-ray diffraction

1
Introduction

Specific structural aspects of inorganic solids often dominate the exploitable properties of the solids. Therefore, many new technological applications require fabrication processes that provide control over the phase, size, morphology and crystallographic orientation of inorganic crystals. The ability of constructing materials organized at nanoscale level from molecular processes is of immediate requirement. Biomineralization processes, or the biological synthesis of inorganic crystals, yield materials with highly regulated structures under moderate conditions of temperature and pressure [1–3]. Furthermore, the crystallochemical specificity of inorganic solids in the biological systems induces so-called self-organized peculiar crystal morphologies. The resultant structural architectures are customized for each property that biological tissues provide. Recently, there has been growing interest in the principles governing the architectures and methods to form a variety of biominerals, such as those found in bones, teeth and shells. Much of this interest stems from the desire to create new highly functionalized synthetic materials, consuming little energy in their production. Owing to serious global environmental problems, all the manufacturing industries are forced to pay more attention to energy consumption. As the understanding of the processes involved in biomineralization developed, researchers have realized a new area of study that takes some inspiration from nature in an effort to construct interesting new structures. Such nature-inspired studies were termed "biomimetics" [4–8]. Indeed, a good deal of the current focus in intelligent materials is centered around mimicking of biological tissues. The formation processes of the biominerals are the results of 40 to 50 million years of fine-tuning by evolution. They must be replete with material scientific key components and the elucidation of biomineralization processes offers valuable insights into material science and engineering.

Biomineralization is characterized by the close association of inorganic and organic substances throughout the entire process. In general biological systems, an organism creates the proper organic matrix on which inorganic crystals can precipitate and the interfacial interactions between them provides the control over the resultant composite structures [3,4,9–11]. The molecular interactions at the inorganic-organic interfaces are an important aspect of biomineralization since the nucleation, growth and organization of biominerals are mediated by the organic supramolecular system.

Calcium phosphate is the main constituent of bone and teeth and is one of the most important biominerals. Hydroxyapatite (HAp), $Ca_5(PO_4)_3OH$, is the most stable calcium phosphate phase in fluids and humid atmospheres under neutral to alkaline conditions [12] and is easily formed in the bodies of vertebrates. There is considerable academic and commercial interest in the development of HAp bioceramics and HAp-loaded polymers for bone replacement. Bone is a nanocomposite material in which collagen fibers are effectively reinforced by an assembly of nano-sized HAp crystallites [13–15]. This structure suggests that bioactive artificial bones such as bone-repairing materials can be essentially obtained through the formation of the nanocomposite structure. Furthermore, the *c*-axes of biological HAp crystallites and the helical axes of the collagen molecules show a strongly preferred orientation along the longitudinal direction of the bone. It is generally accepted that such unique alignment of biological HAp crystallites accompanied with the orientation of collagen fibrils is closely related to macroscopic mechanical properties. The alignment effects of both collagen and HAp on the strength of bone have been investigated experimentally and theoretically, and strong anisotropy in Young's modulus, hardness, fracture strength, bending strength, and fracture toughness has been documented [16–19]. Recently, attempts to fabricate artificial bone materials having bone-like nanostructure and chemical composition have been made [20, 21]. The artificial bone prepared with mimesis of the bone nanostructure can be incorporated into the metabolic system as bone tissue at the recipient sites. The orientated mineralization of HAp crystallites occurs automatically without any physical support by cells. In order to develop new kinds of bioactive materials, it is important to understand the detailed mineralization process of the well-organized bone nanostructure. But it still remains to be clarified from the viewpoint of materials science.

The study of biomineralization, especially on the inorganic-organic interfaces, offers valuable insights into the scope of materials chemistry. However, the interfaces between inorganic-organic materials in living bodies possess such a small and tangled structure that the interfacial interaction cannot be studied directly. Therefore, a model system that can reproduce the inorganic-organic interfaces with simplified structure is required. In this work, as described below, recent attempts to clarify the self-organization mechanism of HAp mineralization through some model systems are reviewed.

2
Organic Matrix-Mediated Crystallization of HAp

2.1
Organic Molecule Assemblages

The tendency for insoluble amphiphilic molecules to accumulate at the gas/solution interface and form highly organized monomolecular films is a physical process that has been widely exploited since the first identification of this phenomenon by Fraulein Pöckels a hundred years ago [22]. For biologists and biophysicists, monolayer films present a versatile and controllable model system that approximates to half the bilayer structure of a biomembrane. In the materials science, interest in the system is linked to the facility for monolayer transfer to solid supports for the formation of multilayers, which have electronics applications [23]. The organic monolayers at the gas/solution interface are called Langmuir films and the organic thin films transferred onto solid substrates are Langmuir–Blodgett (LB) films.

Self-assembled monolayers (SAMs) are surfaces consisting of a single layer of molecules on a substrate [24, 25]. SAMs can be prepared simply by adding a solution of the desired molecule onto the substrate surface and washing off the excess. Common examples are alkane thiol molecules and organosilane molecules chemisorbed onto gold and hydrated oxide surfaces, respectively. Such SAMs are frequently utilized to change physical and chemical properties of surfaces.

An important aspect common to biomineralization processes is the role played by functional groups at the surface of organic crystallization sites. Therefore, for biomineralization researchers, interest has centered on the use of such films as templates for inorganic crystal precipitation. One approach to investigate the inorganic-organic interactions in vitro has been to use the molecular assemblages as organized organic surfaces for inorganic crystallization. When the organic assemblages are placed in simulated body fluids, inorganic crystals precipitate onto the surfaces of the assemblages. Molecules assembled in the above-mentioned forms have been often employed as model organic matrices, such as Langmuir monolayer films [26–43], LB films [44–46], and SAMs [47–52]. Especially, crystallization of calcium carbonate on the organic templates is studied extensively. In the process of calcium carbonate formation in living bodies, the polymorph switching and growth directions are suggested to be controlled by organic membranes. The unexplained mechanism for polymorph switching and directional control has attracted many researchers' interest. As to calcium phosphate crystals represented by HAp, several groups reported that organic functional groups as surface residues of macromolecules are able to induce HAp nucleation [42, 43, 45, 46, 52] and that knowledge is now accepted widely.

2.2
HAp Crystallization on the LB Films

Surfaces of Langmuir films and LB films can be adopted as model systems to study inorganic-organic interfaces, owing to the opportunities to engineer the surface properties (functional group identity, polarity, molecular alignment periodicity, etc.) in a manner that is controllable. In our works, organic monolayer films prepared by the LB method were used to investigate the nucleation mechanism of HAp crystals in a simulated body environment [45, 46]. The LB films with the same functional groups as collagen (i.e., carboxyl groups and amino groups) were placed in a simulated body environment. LB monolayers of arachidic acid ($C_{19}H_{39}COOH$) and stearyl amine ($C_{18}H_{37}NH_2$) were accumulated on fused silica or calcium fluoride (CaF_2) substrates as follows: Arachidic acid or stearyl amine was spread on the water subphase. The obtained organic film on the water surface was slowly compressed up to a surface pressure needed for the ordering of the organic molecules. In the condensed monolayer states, the molecules are closely packed and oriented with their hydrocarbon chains pointing away from the water surface. Subsequently, the monolayer of arachidic acid or stearyl amine was transferred onto a substrate by dipping the substrate into the water subphase; then, the substrate was dropped into the subphase (Fig. 1). The amphiphilic arachidic acid or stearyl amine molecules are standing almost perpendicularly on the substrate and the outermost layer of the LB film is, therefore, occupied by carboxyl groups or amino groups, respectively.

The biomineralization is solidification processes of inorganic ions contained in body fluid. The model system should be constituted from an organic matrix and an adequate aqueous solution. The main constituents of bone are HAp in the form of nanometer-sized crystals and collagen acting as structural protein. When the biomineralization mechanism in natural bone is consid-

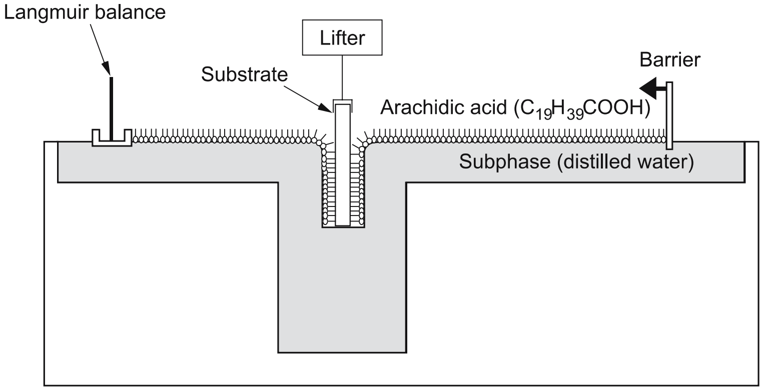

Fig. 1 The trough system for LB film depositions

ered, the surrounding aqueous solution must be the precipitation medium for calcium phosphate crystals. We employed an acellular simulated body fluid (SBF) proposed by Kokubo et al. [53, 54] as the model system for inorganic ions in natural bodies. SBF possesses inorganic ion concentrations and a pH value almost equal to those of human blood plasma. SBF was prepared by dissolving NaCl, $NaHCO_3$, KCl, $K_2HPO_4 \cdot 3H_2O$, $MgCl_2$, $CaCl_2$ and Na_2SO_4 in distilled water and buffered at pH 7.4 with 50 mM of $(CH_2OH)_3CNH_2$ and 45 mM of HCl. The ion concentrations of prepared SBF are given in Table 1. The substrates with the LB films were immersed in SBF for various periods at 36.5 °C and taken out of the fluid. After being gently washed with ion-exchanged distilled water and dried at room temperature, the specimens were evaluated.

The surfaces of fused silica substrates soaked in SBF were subjected to thin-film X-ray diffraction (TF-XRD) measurements. Figure 2 shows the TF-XRD patterns of the LB films. Before soaking a fused silica substrate in SBF, only a broad peak was observed, ascribed to an amorphous structure of glass. In the case of the hydrophobic and hydrophilic glass substrates without LB film, even after being soaked in SBF for 10 days, no appreciable change was detected in the XRD patterns. Similarly, no change in XRD pattern was observed also for the stearyl amine monolayer. However, in the case of the fused-silica substrate with arachidic acid monolayers, new peaks appeared in the XRD pattern after being soaked in SBF; the peaks could be attributed to the apatite or octacalcium phosphate (OCP) structure [55]. Similarity between the diffraction pattern of HAp with low crystallinity and that of OCP at the high angle region prevents the discrimination between HAp and OCP. The most diagnostic 100 diffraction peak of OCP, which is located at almost 4.7°, cannot be identified due to high background. From the results of the XRD measurements, it was indicated that the calcium phosphate crystals could form only on the arachidic acid monolayer but not on the stearyl amine monolayer. In other words, only carboxyl groups could act as a nucleation center for the calcium phosphate formation in SBF.

The surface topography of the crystals grown on the LB films was investigated using a scanning electron microscope (SEM). Figure 3 shows SEM micrographs of the surface with the arachidic acid LB film soaked in SBF for 10 days. The surface of the substrate is partly covered with hemispherical ag-

Table 1 Ion concentrations of simulated body fluid and human blood plasma

	Ion concentration (mM)							
	Na^+	K^+	Ca^{2+}	Mg^{2+}	Cl^-	HCO_3^-	HPO_4^{2-}	SO_4^{2-}
Human blood plasma	142.0	5.0	2.5	1.5	103.0	4.2	1.0	0.5
SBF	142.0	5.0	2.5	1.5	148.3	4.2	1.0	0.5

gregates. SEM micrographs with a higher magnification (Fig. 4) revealed that the hemispherical aggregates are composed of plate-like, curled fragments. At the interface, the crystals are directly attached to the substrate materials as seen in Fig. 4.

The calcium phosphate crystallites were examined by transmission electron microscopy (TEM). Two specimens on fused silica substrates were attached together with epoxy resin; then they were sliced and thinned using argon ion milling as is used for conventional cross-sectional TEM observations [56, 57]. Figure 5a shows the TEM image of the calcium phosphate crystals grown on the LB film surface, which was soaked in SBF for 10 days. The amorphous material at the bottom is the fused silica substrate, on which an aggregate of calcium phosphate nanocrystallites is observed. The nanocrystallites exhibit an elongated plate-like form of 50–100 nm in length and about 10 nm thick. The lattice-fringe image of the nanocrystallites observed is shown in Fig. 5b together with its Fourier transform. The spots indicated by arrows correspond to the periodicity of 0.82 nm, which can be assigned

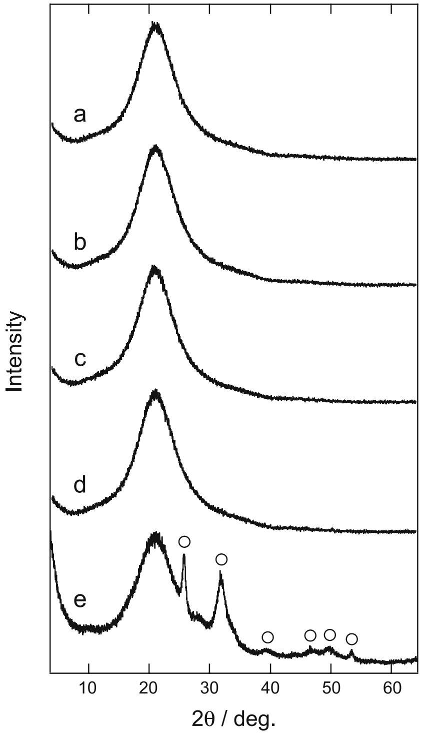

Fig. 2 The TF-XRD patterns of substrates and LB films soaked in SBF for 10 days: **a** hydrophobic glass substrate before soaking; **b** hydrophobic glass substrate; **c** hydrophilic glass substrate; **d** stearyl amine LB film; **e** arachidic acid LB film. (○) Apatite peaks

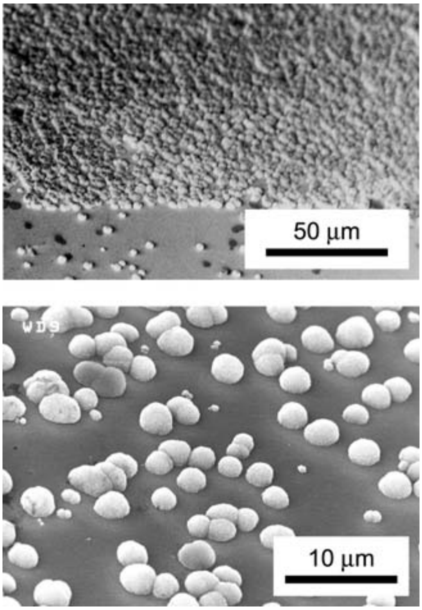

Fig. 3 SEM images of the arachidic acid LB film surface soaked in SBF for 10 days. (Reproduced with permission from [43]. © 2005 The Ceramic Society of Japan)

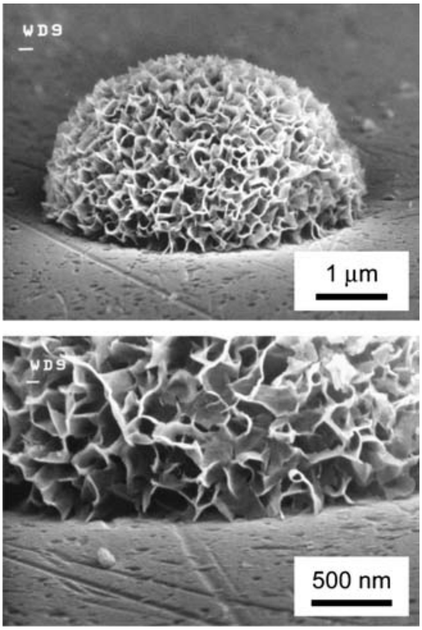

Fig. 4 SEM images of the arachidic acid LB film surface soaked in SBF for 10 days. (Reproduced with permission from [46]. © 2001 Elsevier)

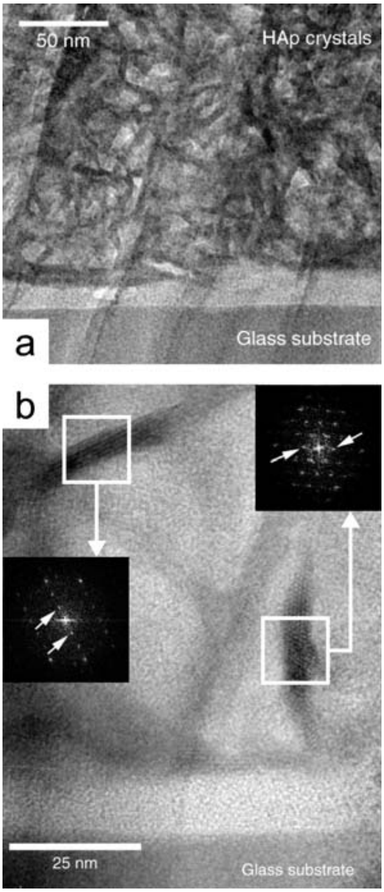

Fig. 5 **a** TEM image of the interface between the LB film and the HAp aggregates. Note that the apparent elongated crystals are in a plate-like form viewed edge-on. **b** Fourier transforms of the lattice-fringes and the corresponding areas are shown. *Arrows* in the Fourier transforms indicate the spots corresponding to the 0.82 nm which is ascribed to the interplanar spacing of {100} in HAp. (Reproduced with permission from [46]. © 2001 Elsevier)

to the interplanar spacing of {100} in the HAp structure [1]. In the right-hand inlet, hexagonal alignment of the spots indicates that the HAp nanocrystallite is oriented with its [001] in parallel to the electron beam. Neither OCP

---

[1] The crystal structure of HAp was ascribed to hexagonal symmetry with the space group $P6_3/m$ by analogy with fluorapatite [58,59]. Elliot et al. [60], however, have revealed that stoichiometric HAp has the space group $P2_1/b$ (monoclinic) at room temperature. Now it is generally believed that pure and stoichiometric HAp is monoclinic [61]. The ordered arrangement of OH ions along the OH columns lowers the symmetry of the HAp crystal structure. The difference between hexagonal and monoclinic symmetry is, however, negligible in the present study and we express the crystal structure according to the hexagonal symmetry

d(100) at 1.86 nm nor its collapsed spacing in vacuum at 1.65 nm [62] was observed during TEM inspection. These results indicate that the crystalline phase on the LB film surface is only HAp. The elongated form of HAp in the TEM images is interpreted to be the cross-section of plate-like shape of the HAp nanocrystallites as revealed in the SEM observation (Fig. 4). Figure 6 shows TEM images of HAp single crystals with lattice fringes and their Fourier transforms. The spots corresponding to the interplanar spacing of

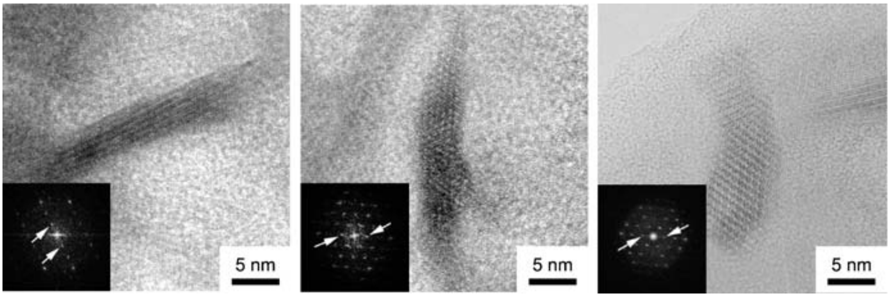

Fig. 6 TEM images of HAp single crystals with lattice fringes and their Fourier transforms. *Arrows* in the Fourier transforms indicate the spots which are ascribed to the interplanar spacing of {100}. Note those spots are found in the direction vertical to the elongated form

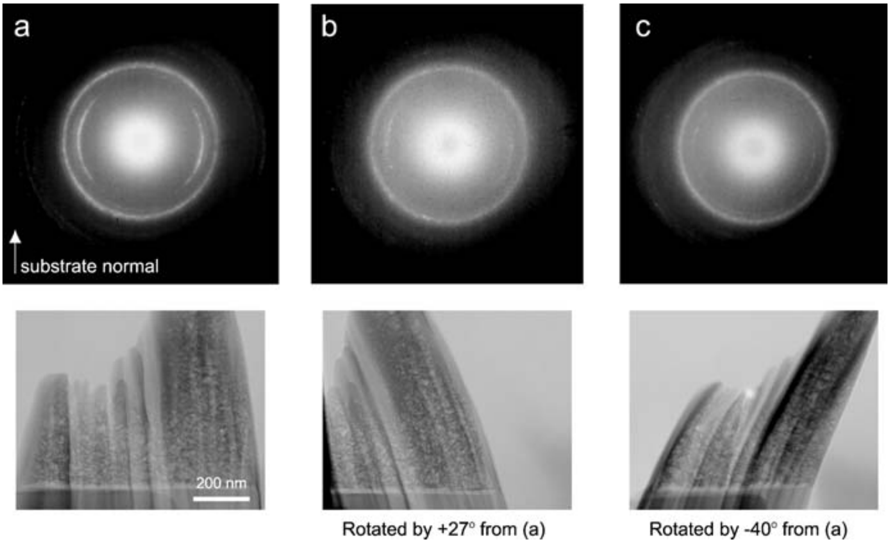

Fig. 7 Change of the selected-area electron diffraction patterns from the HAp crystals near the interface with rotation along the normal of the substrate. The corresponding TEM images are shown below the diffraction patterns. (Reproduced with permission from [46]. © 2001 Elsevier)

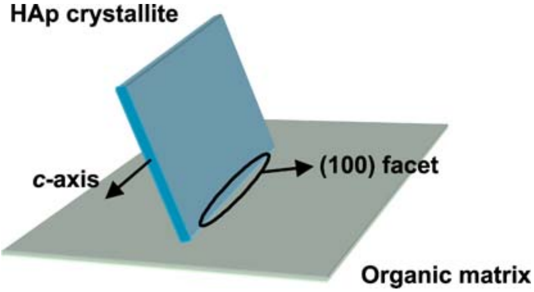

Fig. 8 Schema showing the relationship between the crystallographic property of the HAp crystals and the LB film

0.82 nm are found in the direction vertical to the elongated form, indicating that the plate-like HAp single crystals are parallel to $\{100\}$ planes.

As shown above, carboxyl groups of LB films induced HAp nucleation and HAp crystallite aggregates were formed on the surface of arachidic acid LB monolayer in the simulated body environment. Figure 7a shows the selected area electron diffraction (SAED) patterns taken from an area of ~ 200 nm in diameter inside the HAp aggregate adjacent to the inorganic-organic interface. The Debye ring of the 002 reflection takes a crescent-like form; the direction linking the centers of two crescents is parallel to the interface. As shown in Fig. 7b,c, the diffraction patterns changed with the rotation along the axis normal to the interface; that is, the crescent-like Debye ring gradually disappeared with increasing the rotation angle. This indicates that the *c*-axes of the HAp crystals are preferentially oriented in a specific direction parallel to the interface. If the topography observed by SEM and crystallographic properties elucidated by TEM are taken into consideration, HAp crystal growth on the surface of the LB film, with one of $\{100\}$ faces parallel to the interface, is suggested (Fig. 8). The single crystal could be adjacent to the LB film with the small (100) facet.

2.3
Initial Stage of HAp Nucleation Induced by Carboxyl Groups

As is well known, the body fluid is supersaturated with respect to HAp under the normal condition. Under such an environment, once HAp nuclei are formed, they can grow spontaneously by consuming calcium and phosphate ions from the surrounding body fluid. However, the supersaturation of the body fluid is not so high to induce homogeneous nucleation of HAp [63]. In the above study, nucleation was induced by carboxyl groups on the LB film surface and followed by growth of HAp nanocrystallites. In this section the chemical interactions of inorganic-organic interfaces are analyzed using IR spectroscopy. IR spectroscopy probes the vibrational features of organic molecules. Developments in Fourier transform IR (FT-IR) techniques have increased the sensitivity sufficiently so as to observe reliable IR spectra at the monomolecular layer level. Therefore, IR spectroscopy provides a convenient and useful way for the analysis of constituent groups in a LB film. A CaF_2 crystal is transparent in the wavelength region from 0.13 to 12.0 μm. The LB film formed on the CaF_2 substrates were subjected to IR transmission spectral measurement.

Figure 9 shows IR transmission spectra of the arachidic acid LB film at several soaking stages. A strong absorption peak found at $1702\,\mathrm{cm}^{-1}$ for the specimen before soaking in SBF (Fig. 9a) is assigned to the stretching mode of $C = O$ in a carboxyl group. The observation of this peak indicates that the arachidic acid molecules without covering of inorganic ions kept a nonionized state COOH. After soaking in SBF for 1 h, as shown in Fig. 9b, the $C = O$ stretching peak entirely disappeared while antisymmetric $-CO_2^-$ stretching peaks appeared at 1576 and $1543\,\mathrm{cm}^{-1}$, indicating that the carboxyl group was ionized by adsorbing ions in SBF. After soaking in SBF for 24 h (Fig. 9c), some

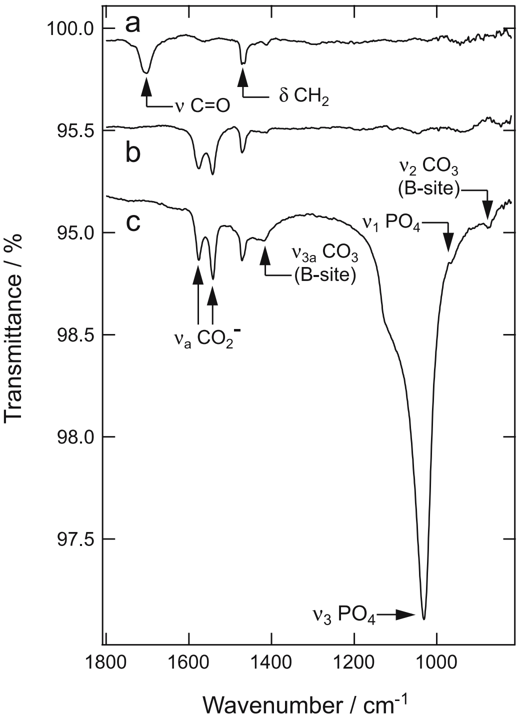

Fig. 9 IR transmission spectra of an arachidic acid LB film and samples soaked in SBF. **a** Before soaking; **b** after being soaked in SBF for 1 hour; **c** after being soaked in SBF for 24 hours. The spectra are offset for clarity. (Reproduced with permission from [46]. © 2001 Elsevier)

IR peaks ascribed to HAp containing carbonate ions appeared: i.e., 965 cm^{-1} and 1031 cm^{-1} for PO_4, 875 cm^{-1} and 1413 cm^{-1} for CO_3^{2-} [64, 65]. Although CO_3 ions can replace both the OH site (A site) and the PO_4 site (B site) in the HAp structure, the CO_3 peaks shown in Fig. 9c are assigned only to the B site. It is known that the CO_3 substitution at the A site in HAp crystals is limited to the preparation in aqueous systems, as has been proved in the present study [55]. The nanocrystallites grown on the LB film surface exhibit a plate-like morphology reminiscent of OCP, which may form as a transient phase because of the relatively high supersaturation of SBF. TEM observation showed that the deposited crystals have HAp structure. As shown in the results of the IR spectra measurement, the crystals precipitated on the LB films are B-type carbonate HAp. It is reported that carbonate ions incorporated in HAp can cause reduction in crystallinity (decrease in crystal size) and change morphology to flatten crystals with hexagonal symmetry maintained [66].

Figure 10 shows the IR transmission spectra of arachidic acid monolayers soaked in various solutions. After soaking in SBF for 1 h, as shown in Fig. 9b, a $C = O$ stretching peak vanished while an antisymmetric $-CO_2^-$ stretching peak correspondingly appeared. It is worthwhile to note that the $-CO_2^-$ stretching vibration formed a doublet at 1576 and 1543 cm^{-1}. Figure 10 gives the IR spectra of the arachidic acid monolayers soaked in an aqueous solution containing Ca^{2+} and/or Na^+ (Fig. 10b–d). Compositions of LB film aqueous soaking solutions are presented in Table 2. When the LB films were soaked in $CaCl_2$ and/or NaCl solutions, a $C = O$ stretching absorption peak could be found at 1702 cm^{-1}, indicating the existence of nonionized COOH, and an antisymmetric $-CO_2^-$ stretching peak was simultaneously found as a broad singlet at 1558 cm^{-1}. Figure 10e shows the IR spectrum of the arachidic acid LB film soaked in $CaCl_2$ aqueous solution for 1 h and subsequently in K_2HPO_4 aqueous solution for 1 h. The antisymmetric $-CO_2^-$ stretching peak showed a doublet at the same wavenumber region as that of the SBF-soaked monolayer.

The arachidic acid LB film surface is negatively charged under the simulated body environment, as determined from zeta-potential measurements[2]. The cations should first adsorb on the carboxyl groups; therefore, when the monolayer was soaked in $CaCl_2$ or NaCl solutions, the divalent Ca^{2+} ion or monovalent Na^+ ion could be adsorbed on it. In the $CaCl_2$/NaCl mixed solution the divalent and monovalent cations could both adsorb on the arachidic acid monolayer. The IR spectra for the monolayers soaked in $CaCl_2$ and/or

---

[2] We evaluated the zeta-potentials of the LB films in the simulated body environment. The values of arachidic acid and stearyl amine monolayers were – 61 and + 41 mV, respectively, while that of the fused silica substrate without LB monolayer was – 41 mV. The negative zeta-potential for the arachidic acid monolayer corresponded to a charged group $-CO_2^-$ and the positive potential for the stearyl amine monolayer corresponded to a charged group $-NH_3^+$. The electrostatic properties of the LB monolayer surfaces depend on the functional groups

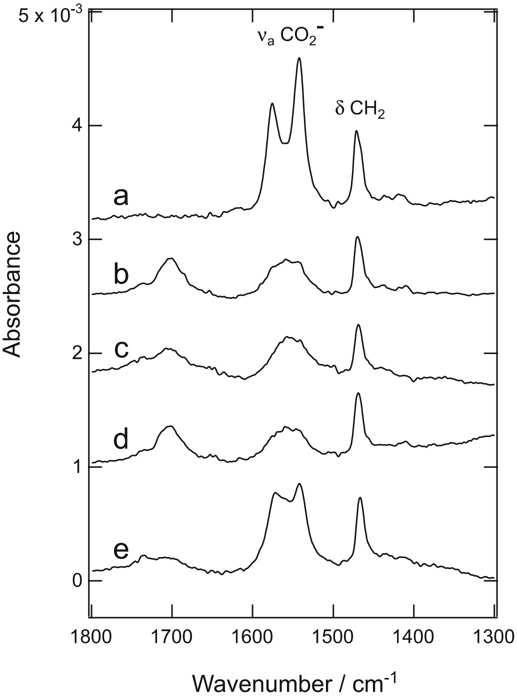

Fig. 10 IR transmission spectra of arachidic acid LB films soaked in various solutions: **a** SBF for 1 hour; **b** $CaCl_2$ solution for 1 hour; **c** NaCl solution for 1 hour; **d** $CaCl_2$ and NaCl solution for 1 hour; **e** $CaCl_2$ solution for 1 hour and subsequently in K_2HPO_4 solution for 1 hour. The spectra are offset for clarity. (Reproduced with permission from [45]. © 2000 Wiley)

Table 2 Compositions of LB film aqueous soaking solutions

	Compound	Concentration (mM)
Solution 1	$CaCl_2$	2.5
Solution 2	NaCl	5.0
Solution 3	$CaCl_2$	2.5
	NaCl	5.0
Solution 4	K_2HPO_4	1.0

NaCl solutions were almost identical but very different from the IR spectra for the monolayers soaked in calcium and phosphoric ion containing solutions. When the arachidic acid LB film covered with Ca^{2+} was soaked in K_2HPO_4 solution, phosphoric ions could adsorb on the Ca^{2+} layer. Therefore, the doublet with the splitting of 33 cm^{-1} in the $-CO_2^-$ stretching peak was ascribed to the effect of *low site symmetry* because of the adsorption of calcium ions followed by the adsorption of phosphoric ions, which reduced the symmetry of $-\mathrm{CO_2}^-$. In SBF the calcium and phosphoric ions could adsorb on the carboxylate layer, resulting in the HAp nucleation process.

It was shown that crystallization of HAp was induced by the chemical interaction between carboxyl groups and inorganic ions in the body fluid. The carboxyl group could adsorb calcium ion and subsequently phosphoric ion upon itself. This is thought to be the initial process of HAp nucleation.

2.4

In-Situ IR Spectral Measurement in HAp Crystallization

As the controlling mechanism of biominerals' crystallographic orientations, two potential models, a geometric model and a stereochemical model have been investigated [3, 4]. The geometric model is based on the idea that the close matching between lattice spacing in certain crystal faces and distances that separate functional groups periodically arranged on the organic surface determines the crystallographic features. The stereochemical model can be described as follows: when inorganic ions bind to the organic matrices, the resultant atomic arrangement around each organic functional group binding inorganic ions resembles the specific crystal structure to such an extent that the interfacial energy associated with nucleation of the crystal is specifically lowered. However, macromolecules often display considerable molecular dynamics in their surface residues as well as along the polypeptide or polysaccharide backbone. The static models should be inadequate to examine the biomineralization processes in a comprehensive manner. Accordingly, to reveal the principles governing biomineralization processes, behaviors of the organic matrix during the biominerals formation should be studied. In the present work, we attempted to study the HAp nucleation process in-situ. We employed IR external reflection spectroscopy for the in-situ analysis of the nucleation process. The external reflection spectroscopy is a powerful tool to probe the structures of organic thin films at air-water interfaces [28, 67, 68]. Structural changes of Langmuir monolayer films with carboxyl groups, which are capable of inducing HAp nucleation, were studied during HAp crystallization.

Arachidic acid was spread on a subphase of distilled water or SBF. The residual organic film upon the subphase (Langmuir monolayer film) was subjected to the in-situ IR spectra measurement. A Langmuir trough was built into a grazing angle accessory in the sample chamber of an IR spectrometer, and the external reflection spectra for the organic thin films at the air-solution interfaces were recorded (Fig. 11). The incident beam was nonpolarized and irradiated at the air-solution interfaces at a near-normal incidence (10°). The spectrum obtained with the film was ratioed with the background spectrum collected without the film.

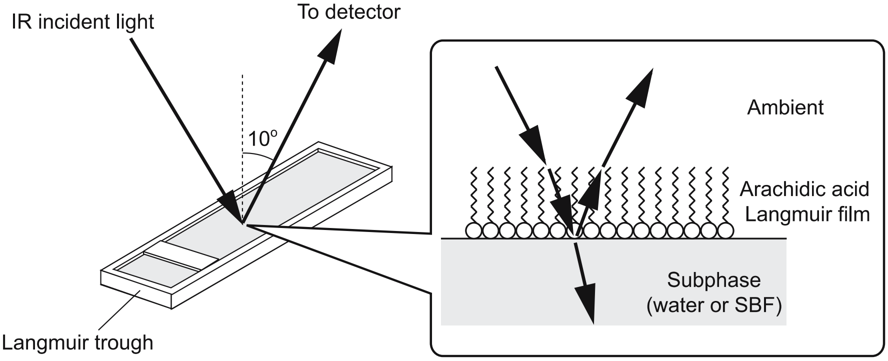

Fig. 11 Schema of the IR external reflection spectroscopy accessory

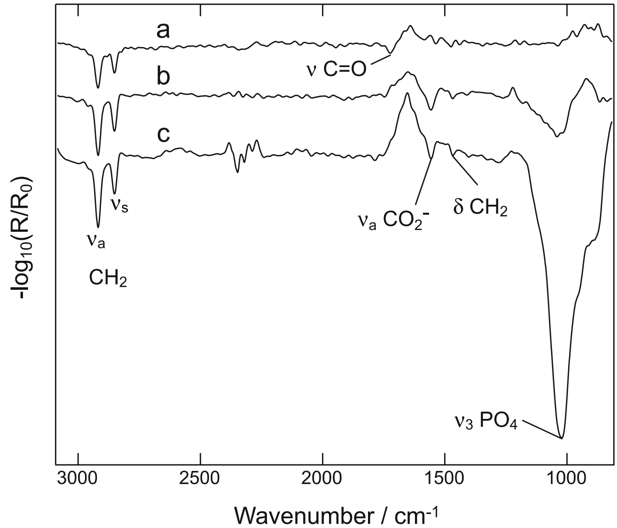

Fig. 12 IR external reflection spectra of arachidic acid Langmuir monolayer film: **a** on pure water subphase; **b** on SBF; **c** 12 hours later of **b**. (Reproduced with permission from [43]. © 2005 The Ceramic Society of Japan)

Figure 12 gives IR spectra of arachidic acid monolayer films spread on pure water and SBF. In the absorption band found in the 2800–3000 cm^{-1} region, the peaks at 2920 and 2850 cm^{-1} were assigned to the antisymmetric and symmetric vibrations of the methylene groups ($-CH_2-$), respectively. Theoretical calculations using classical electromagnetic theory have been studied for organic thin films at the air-solution interfaces [69, 70]. At 10° incidence, the condition used in the present study, the *E* field of the light is parallel to the solution surface. Hence, vibrations that have dipole moments parallel to the surface are preferentially observed. The dipole moments of the methylene groups' vibrations are perpendicular to the alkyl chain axis of the arachidic acid molecule. Therefore, the alkyl chains should be rather vertical on the surfaces of the subphase. The appearance of these absorption bands means that the Langmuir monolayer film of arachidic acid was successfully formed on the subphase.

As to the Langmuir film on the pure water, an absorption band was found around 1700 cm^{-1}, which was assigned to the stretching mode of $C = O$ in a carboxyl group. This band indicates that the arachidic acid molecules on the pure water subphase were not ionized entirely but some molecules were kept in a nonionized state – COOH. In Fig. 12b, a $C = O$ stretching band vanished while an antisymmetric – CO_2^- stretching band correspondingly appeared, indicating that the carboxyl groups were ionized by adsorbing ions in SBF. In the spectrum, an IR band ascribed to PO_4 was also found at 1030 cm^{-1}. The spectrum from the Langmuir film laid upon the SBF subphase for 12 hours is shown as Fig. 12c. The absorption band ascribed to PO_4 grew much stronger, indicating that HAp crystal nucleation had proceeded below the Langmuir film. These results agree with our knowledge that the carboxyl groups in the Langmuir monolayer film act as nucleation centers for HAp crystals formation.

Spectra of the $C-H$ stretching region taken during the HAp nucleation process are shown in Fig. 13. Concurrently with the HAp nucleation, the intensities of the antisymmetric and symmetric methylene stretching vibrations varied with time, while their peak positions remain the same. The serial

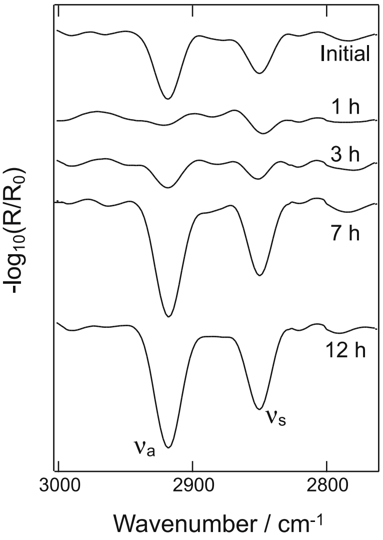

Fig. 13 Spectral changes in $C-H$ stretching region during HAp crystallization under arachidic acid Langmuir monolayer film at the air-solution (SBF) interface. The elapse times are initial (0 hour), 1 hour, 3 hours, 7 hours and 12 hours from *top* to *bottom*. (Reproduced with permission from [43]. © 2005 The Ceramic Society of Japan)

change in the absorption intensities did not occur when the Langmuir film is placed upon a pure water subphase, and should be a characteristic phenomenon of the Langmuir films below which HAp nucleation proceeds. The C – H stretching band intensities shrank to almost nothing at 1 hour after crystallization started, and then increased again to become larger than the initial state. The intensities of the antisymmetric and symmetric vibrations of the methylene groups decreased, indicating that the alkyl chains reoriented away from the subphase surface normal. The changes in the C – H stretches indicate the occurrence of conformation changes in the Langmuir film. For long-chain hydrocarbon molecules, the wavenumbers of the antisymmetric and symmetric vibrations are conformation sensitive due to perturbation by Fermi resonance, and that they can be correlated with the ordering of the hydrocarbon chains. Lower wavenumbers are characteristic of highly ordered all-*trans* conformations, while the number of gauche conformation (the disorder of the chains) increases with increasing wavenumbers [71, 72]. The peak positions of the methylene groups' vibrations in this experiment, 2920 and 2850 cm^{-1}, correspond to ordered all-*trans* conformations. Throughout the structural change of Langmuir monolayer film associated with HAp nucleation, no distortion in the molecular structure of arachidic acid was detected. Hence, the conformation changes in the Langmuir film was not triggered by intermolecular interactions among alkyl chains. Arachidic acid molecules incorporated in the Langmuir film are facing the SBF surface directly with their carboxyl groups, and the carboxyl groups act as nucleation centers for HAp. The adsorption of calcium ions to carboxyl groups followed by the adsorption of phosphoric ions results in the formation of embryonic clusters of ions. When the expenditure of the free energy required for creating a new interface is overcome by the energy released in the formation

Fig. 14 Schema showing the probable HAp nucleation process mediated by the arachidic acid monolayer and associated structural change of the organic monolayer. (Reproduced with permission from [43]. © 2005 The Ceramic Society of Japan)

of chemical bonds in the solid phase, the embryonic clusters can act as the HAp crystal nuclei and spontaneous crystal growth occurs. With the formation of embryonic clusters composed of carboxyl groups and inorganic ions, the hydrocarbon chains connected to the carboxyl groups should change their conformation, i.e., their positions or inclinations to the SBF surface (Fig. 14). The present result implies that the organic matrices change their structures to induce HAp nucleation, and adapt themselves to optimize geochemical or stereochemical fit to the grown HAp crystals.

The present study revealed that organic matrices that can induce HAp nucleation change their structures during HAp crystallization. The organic matrices should not be treated as a rigid template, but their structural changes associated with the formation of crystal embryos should be taken into account, when the biomineralization mechanism is discussed. At least, the matching between lattice spacing in crystal faces and periodicity in functional group arrangement on the organic surfaces should not be the principal cause of the crystallographic features determination.

3

Atomic Scale $\{100\}$ Interfacial Structure in HAp

To enable discussion on the interfacial interactions between HAp and organic substances, a thorough understanding of the surface structure and composition of HAp is fundamental. Apart from the importance of HAp as a constituent of biomimetic materials, surface structure determination of HAp is still very significant for the basic understanding of this material. For instance, morphology of crystals is generally dominated by the surface energy states of crystal faces. The surface energy states cannot be discussed without the knowledge of the atomic structure. Although the bulk structure of HAp has been extensively studied, the surface structure of HAp is poorly studied. Recent developments in surface science are clarifying surface structures of various materials at atomic scale. However, the complexity of the crystal structure, lack of electric conductivity and weakness against various probes prevent the study of the surface structure of HAp.

Both natural and synthetic HAp crystals are often facetted with the possible six equivalent faces, expressed as $\{100\}$ planes in hexagonal symmetry. As described in Sect. 2.2, carboxyl groups can react to the $\{100\}$ surfaces of HAp during its crystallization process. Hence, the surface structure of $\{100\}$ planes is especially important. We have investigated the structural termination of sintered HAp crystals at the interfaces parallel to the $\{100\}$ plane using high-resolution transmission electron microscopy (HRTEM) [73]. We examined crystalline-amorphous interfaces formed by the electron beam damage, and grain boundaries parallel to $\{100\}$. These structures must be related to a stable atomic arrangement of the $\{100\}$ surfaces of HAp.

Synthetic HAp powder was sintered to be a dense specimen. XRD study indicated that the specimen consisted of only apatite as a crystalline phase. The FT-IR spectrum showed absorption bands at 3570 and 630 cm^{-1} which are ascribed to the hydroxyl stretching and librational modes in HAp, respectively [64]. No absorption band related to carbonate ions was observed [74]. As a result, it was confirmed that the specimen was pure HAp, carbonate-free and not dehydrated by sintering. Sintered HAp was polished mechanically, and thinned to electron transparency by argon ion-milling. HRTEM observations were performed at 200 kV of accelerating voltage. Details in the obtained images were interpreted to provide atomic information by comparison with multi-slice simulated images [75]. The simulated images were calculated using MacTempas software (Total Resolution Co).

Figure 15 shows a view of the HAp structure observed down to [001] and Fig. 16 indicates corresponding simulated HRTEM images as functions of defocus values and specimen thickness. The simulated images were calculated at two defocus values. Hexagonally arranged bright spots which correspond to Ca1 sites are distinctive at the defocus value around – 42 nm (Scherzer defocus) with the specimen thickness larger than 7.5 nm. These bright contrasts are due to dense packing of Ca ions along the [001] direction (hereafter referred as Ca1 columns). On the other hand, a characteristic hexagonal pinwheel-like contrast appears around OH columns in the structure when the defocus value is around – 5 nm and the specimen thicker than 10 nm [76]. These two characteristic features are useful to make correspondence between the image contrasts and the atomic structure of HAp. In the following section, the former focusing condition is referred as DF1 and the latter as DF2.

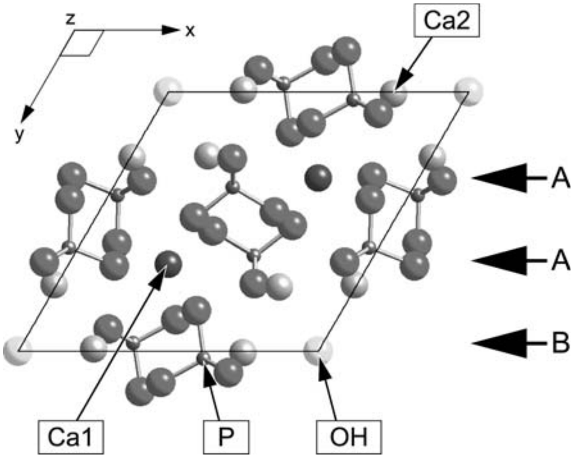

Fig. 15 HAp crystal structure observed along ⟨001⟩. The planes "A" and "B" are the possible positions where a HAp structure can be terminated

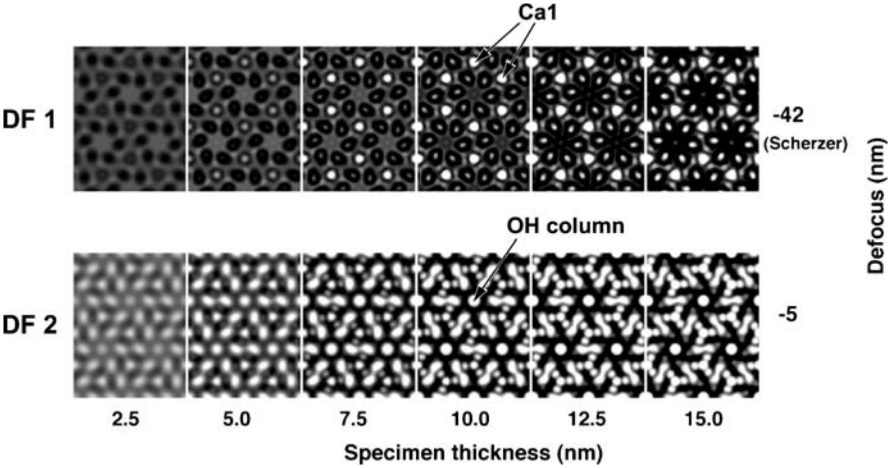

Fig. 16 HRTEM images simulated for a HAp structure along ⟨001⟩: multislice simulations were performed at two defocus values (DF). The *hexagonally arranged bright spots* at *DF* = – 42 nm (Scherzer defocus) correspond to Ca1 sites. A characteristic pinwheel contrast corresponding to the OH column appears at *DF* = – 5 nm. (Reproduced with permission from [73]. © 2002 The American Ceramic Society)

When a HAp crystal was oriented as its ⟨001⟩ direction was parallel to the incident beam and observed at high magnification, characteristic radiation damage was formed in the crystal by the electron beam. Figure 17 shows a HRTEM image (DF1 condition) of the damaged crystal formed by radiation lasting a few minutes with a beam current density of 1–2 A/cm^2 on the specimen. Hexagonally shaped areas, whose boundaries are parallel to $\{100\}$, are observed in which the material is amorphized. Examination of the contrast in the remaining crystal adjacent to the boundaries indicates that the crystal thickness is at least 5–10 nm. As a result the amorphized regions are regarded as three-dimensional hexagonal prisms surrounded by $\{100\}$ planes of the HAp crystal. Such hexagonally shaped damaged regions in HAp have already been reported [77]. However, it is not possible to discuss the atomic structure at the interfaces as described below until sharp HRTEM images such as those shown in this work are available. Figure 18 represents a HRTEM image (DF2 condition) of a considerably damaged area. The contrasts at several interfaces between crystalline and amorphous regions (indicated by the arrowheads in the figure) are almost identical. It is also observed in several places that the contrast in the crystalline region is sharply changed with the $\{100\}$ plane as the boundary, suggesting that the crystal thickness is step-likely changed.

Figure 19a shows a magnified image at one of the $\{100\}$ crystalline-amorphous interfaces indicated by the arrowheads in Fig. 18. To determine the terminated structure of HAp in this image, we performed the multi-slice image simulations using artificial large unit cells where almost the upper half

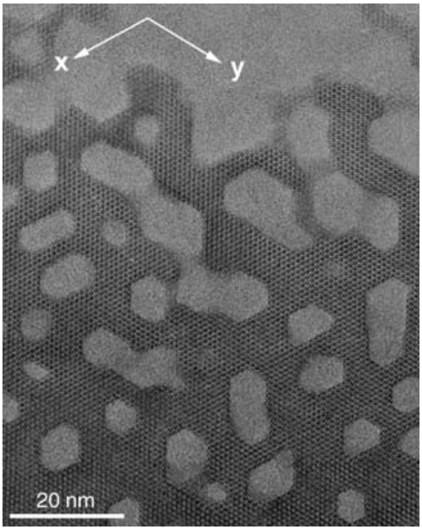

Fig. 17 HRTEM image observed for a HAp crystal in which the electron radiation damage occurred: the beam direction is ⟨001⟩. The defocus is close to the Scherzer conditions. (Reproduced with permission from [73]. © 2002 The American Ceramic Society)

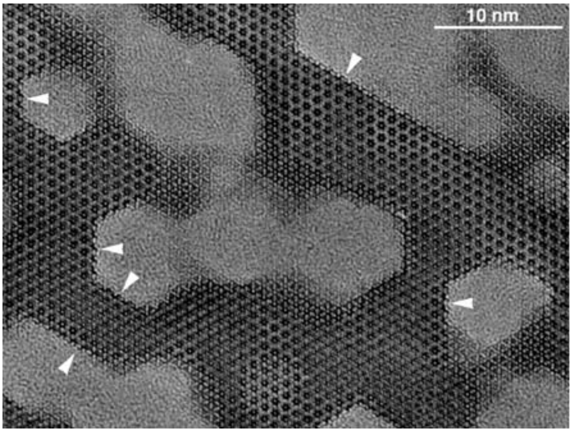

Fig. 18 HRTEM image of electron radiation damage in HAp at $DF = -5$ nm. Notice that the contrasts at the boundaries of the crystal, indicated by the *arrowheads*, are almost identical. (Reproduced with permission from [73]. © 2002 The American Ceramic Society)

is vacant and the lower is the atomic arrangement of HAp with various terminations. Figure 19b,c indicates the simulated image of the $\{100\}$ interface that agrees best with the experimental one (Fig. 19a) and the termination model used in the simulation, respectively. At the interface, the HAp crystal struc-

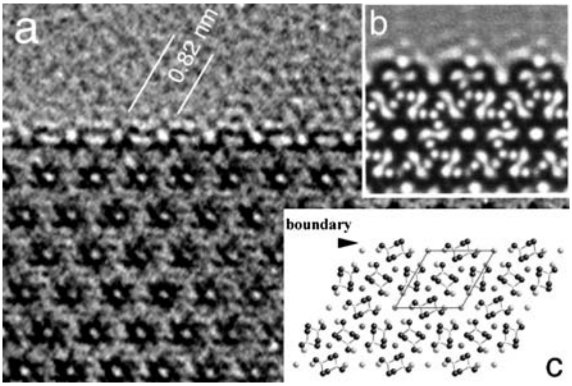

Fig. 19 Observed (**a**) and simulated (**b**) images of the {100} boundary of HAp. The **b** image was calculated using the boundary structure model at the *bottom right* of the figure (**c**). (Reproduced with permission from [73]. © 2002 The American Ceramic Society)

ture is terminated with the plane on which the OH columns, Ca2 site and PO_4 tetrahedra exist. Simulation images for structure models without outermost OH ions or oxygen atoms coordinating Ca2 and P were identical to Fig. 19b because of their weak charge potential. Therefore, for instance, whether OH ions reside in the outermost OH columns or not cannot be discussed.

In addition to the crystalline-amorphous interfaces formed by radiation damage, we tried to determine the atomic structure of the {100} planes at the grain boundaries in the specimen. Figure 20 shows a result of HRTEM recording at the grain boundary where the lower grain is aligned along ⟨001⟩ and attached to the upper grain with stepped {100} planes. The original image, which was recorded at the DF1 condition, was compressed to one third in the horizontal direction to make the boundary clear. The lattice fringe in the upper grain reaches to the grain boundary, indicating the boundary was not damaged during the observation and recording. The {100} terraces in the HAp structure are terminated with the specific contrast as indicated by the arrowheads in Fig. 20. The tracing from the inside of the crystal revealed that a pair of horizontal white dot rows (denoted "A" at the left of the figure) corresponds to Ca1 columns and OH columns locate at the dark lines ("B") between them (see also Fig. 15). The contrasts of the {100} terraces at the boundaries are all at these dark lines, suggesting the HAp structure is terminated at the plane connecting the OH columns. This result is the same as that obtained at the crystalline-amorphous interfaces as described above.

The atomic arrangement observed at the crystalline-amorphous interface and grain boundary is probably one of the stable structures for the {100} surface of HAp. This terminated structure is the same as the edge of the cluster model in amorphous calcium phosphate proposed from X-ray diffraction study [78]. When the HAp structure is amorphized by electron beam radia-

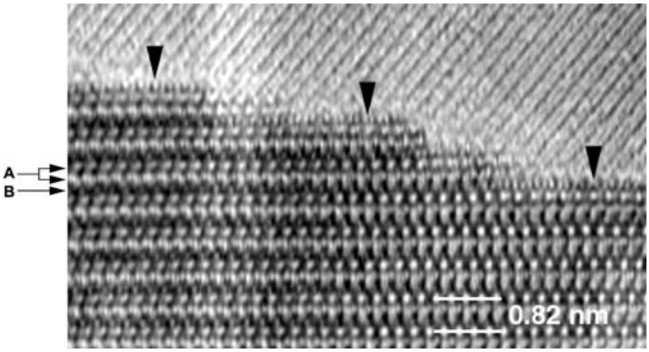

Fig. 20 HRTEM image of a grain boundary in HAp. The original image was compressed to one-third in the horizontal direction to make the boundary structure clear. The planes denoted "A" and "B" correspond to those given in Fig. 15. (Reproduced with permission from [73]. © 2002 The American Ceramic Society)

tion, or when the crystal growth proceeds on {100} facets by sintering, the crystal may be broken and grow with this cluster like a block. It has also been proposed that clusters of similar size exist in solutions supersaturated with HAp and the HAp crystal in the solutions grows by adsorption of the clusters [79].

We observed the crystalline-amorphous interfaces and the grain boundaries of sintered HAp by HRTEM. When the interfaces or boundaries are parallel to {100}, both of them showed the same atomic arrangement for the termination of the HAp crystal. The crystal structure of HAp is terminated at a plane crossing the OH columns on which Ca2 sites and PO_4 tetrahedra are located. This atomic arrangement for the {100} surfaces of HAp probably has a low surface energy and may be common in HAp crystals formed by various conditions.

4
Concluding Remarks

When the results of above mentioned HAp crystallization experiments on the organic molecule assemblages and the knowledge withdrawn from the HRTEM observations are combined, a model for HAp crystals nucleation and growth can be developed (Fig. 21). Carboxyl groups on the organic matrices act as nucleation centers for HAp. The carboxyl groups could adsorb inorganic ions upon themselves; especially calcium ions and phosphoric ions were adsorbed in the body environment. The resultant embryonic clusters of ions composed of the carboxyl group, calcium and phosphoric ions are the origination of HAp formation. The embryo could correspond to the Ca2 site and PO_4 tetrahedron on the most stable HAp {100} surface, and the HAp crystals

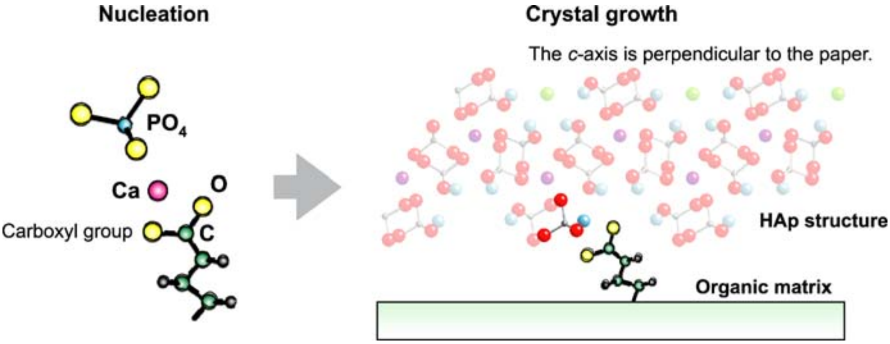

Fig. 21 The mechanism of HAp mineralization proposed in view of the experimental results

grow with their {100} surfaces parallel to the interface. Actually, changes in bond energies caused by water molecules mediation, lattice relaxations of the crystal surface structure, and molecular movements in the surface residues of the organic matrices might result in more complex phenomena at the interface. Continued investigations on this issue are expected to offer further valuable insights into biomimetic materials chemistry.

Acknowledgements I am pleased to acknowledge the collaborators who have supported and nurtured this work, in particular, Prof. Junzo Tanaka (Tokyo Institute of Technology), Prof. Toshihiro Kogure (University of Tokyo) and Ms. Yuri Kumagai (Japan Science and Technology Agency, CREST). More recently, the support of Dr. Koji Watari (AIST) has been significant.

References

1. Addadi L, Weiner S (1992) Angew Chem Int Ed Engl 31:153
2. Weiner S, Addadi L, Wagner HD (2000) Mat Sci Eng C 11:1
3. Mann S (2001) Biomineralization: principles and concepts in bioinorganic materials chemistry. Oxford University Press, New York
4. Mann S (1996) Biomineralization and biomimetic materials chemistry. In: Mann S (ed) Biomimetic materials chemistry. VCH Publishers, New York, p 1
5. Dujardin E, Mann S (2002) Adv Mater 14:775
6. Estroff LA, Hamilton AD (2001) Chem Mater 13:3227
7. Li C, Kaplan DL (2003) Curr Opin Solid State Mat Sci 7:265
8. Sarikaya M, Tamerler C, Jen AKY, Schulten K, Baneyx F (2003) Nature Mater 2:577
9. Mann S, Archibald DD, Didymus JM, Douglas T, Heywood BR, Meldrum FC, Reeves NJ (1993) Science 261:1286
10. Mann S (1993) Nature 365:499
11. Mann S (1988) Nature 332:119
12. Aoki H (1992) Science and medical applications of hydroxyapatite. Ishiyaku-Euro America, Tokyo
13. Jackson SA, Cartwright AG, Lewis D (1978) Calcif Tiss Res 25:217

14. Posner AS (1985) Clin Orthop Rel Res 200:87
15. Bloom W, Fawcett DW (1994) Bone. In: A textbook of histology. Chapman & Hall, New York, p194
16. Bonfield W, Grynpas MD (1977) Nature 270:453
17. Katz JL (1980) Nature 283:106
18. Sasaki N, Matsushima N, Ikawa T, Yamamura H, Fukuda A (1989) J Biomech 22:157
19. Wagner HD, Weiner S (1992) J Biomech 25:1311
20. Kikuchi M, Itoh S, Ichinose S, Shinomiya K, Tanaka J (2001) Biomaterials 22:1705
21. Kikuchi M, Matsumoto HN, Yamada T, Koyama Y, Takakuda K, Tanaka J (2004) Biomaterials 25:63
22. Petty MC (1996) Langmuir-Blodgett films: an introduction. Cambridge University Press, New York
23. Roberts G (ed) (1990) Langmuir-Blodgett films. Plenum Press, New York
24. Sagiv J (1980) J Am Chem Soc 102:92
25. Ulman A (1991) An introduction for ultrathin organic films: from Langmuir-Blodgett to self-assembly. Academic Press, San Diego
26. Heywood BR, Mann S (1992) Adv Mater 4:278
27. Heywood BR, Mann S (1994) Adv Mater 6:9
28. Berman A, Ahn DJ, Lio A, Salmeron M, Reichert A, Charych D (1995) Science 269:515
29. Zhao XK, Yang J, McCormick LD, Fendler JH (1992) J Phys Chem 96:9933
30. Lin H, Sakamoto H, Seo WS, Kuwabara K, Koumoto K (1998) J Crystal Growth 192:250
31. Heywood BR, Mann S (1994) Chem Mater 6:311
32. Mann S, Heywood BR, Rajam S, Walker JBA (1991) J Phys D Appl Phys 24:154
33. Rajam S, Heywood BR, Walker JBA, Mann S, Davey RJ, Birchall JD (1991) J Chem Soc Faraday Trans 87:727
34. Heywood BR, Rajam S, Mann S (1991) J Chem Soc Faraday Trans 87:735
35. Heywood BR, Mann S (1992) J Am Chem Soc 114:4681
36. Mann S, Heywood BR, Rajam S, Birchall JD (1988) Nature 334:692
37. Volkmer D, Fricke M, Vollhardt D, Siegel S (2002) J Chem Soc Dalton Trans 4547
38. Ahn DJ, Berman A, Charych D (1996) J Phys Chem 100:12455
39. Berman A, Charych D (1999) J Crystal Growth 198/199:796
40. Berman A, Charych D (1999) Adv Mater 11:296
41. Buijnsters PJJA, Donners JJJM, Hill S, Heywood BR, Nolte RJM, Zwanenburg B, Sommerdijk NAJM (2001) Langmuir 17:3623
42. Lin H, Seo WS, Kuwabara K, Koumoto K (1996) J Ceram Soc Japan 104:291
43. Sato K, Kumagai Y, Ikoma T, Watari K, Tanaka J (2005) J Ceram Soc Japan 113:112
44. Sato K, Kumagai Y, Watari K, Tanaka J (2004) Langmuir 20:2979
45. Sato K, Kumagai Y, Tanaka J (2000) J Biomed Mater Res 50:16
46. Sato K, Kogure T, Kumagai Y, Tanaka J (2001) J Col Int Sci 240:133
47. Küther J, Seshadri R, Knoll W, Tremel W (1998) J Mater Chem 8:641
48. Travaille AM, Donners JJJM, Gerritsen JW, Sommerdijk NAJM, Nolte RJM, Kempen HV (2002) Adv Mater 14:492
49. Küther J, Tremel W (1997) Chem Commun 2029
50. Küther J, Tremel W (1998) Thin Solid Films 327–329:554
51. Han YJ, Aizenberg J (2003) J Am Chem Soc 125:4032
52. Tanahashi M, Matsuda T (1997) J Biomed Mater Res 34:305
53. Kokubo T, Ito S, Huang ZT, Hayashi T, Sakka S, Kitsugi T, Yamamuro T (1990) J Biomed Mater Res 24:331

54. Kokubo T, Kushitani H, Sakka S, Kitsugi T, Yamamuro T (1990) J Biomed Mater Res 24:721
55. Elliott JC (1994) Structure and chemistry of the apatites and other calcium orthophosphates. Elsevier Science, Amsterdam
56. Kogure T (1997) Mineral J 19:155
57. Kogure T, Murakami T (1998) Am Mineral 83:358
58. Posner AS, Perloff A, Diorio AF (1958) Acta Crystallogr 11:308
59. Kay MI, Young RA (1964) Nature 204:1050
60. Elliot JC, Mackie PE, Young RA (1973) Science 180:1055
61. Young RA, Holcomb DW (1982) Calcif Tissue Int 34:S17
62. Nelson DGA, McLean JD (1984) Calcif Tissue Int 36:219
63. Ohtsuki C, Kokubo T, Yamamuro T (1992) J Non-Cryst Solids 143:84
64. Fowler BO (1974) Inorg Chem 13:194
65. Suetsugu Y, Shimoya I, Tanaka J (1998) J Am Ceram Soc 81:746
66. LeGeros RZ (1994) Biological and synthetic apatites. In: Brown PW, Constantz B (eds) Hydroxyapatite and related materials. CRC Press, Boca Raton, p 3
67. Sakai H, Umemura J (1993) Chem Lett 2167
68. Sakai H, Umemura J (2002) Colloid Polym Sci 280:316
69. Dluhy RA (1986) J Phys Chem 90:1373
70. Fina LJ, Tung Y-S (1991) Appl Spectrosc 45:986
71. Gericke A, Hühnerfuss H (1994) Thin Solid Films 245:74
72. Gericke A, Hühnerfuss H (1995) Langmuir 11:225
73. Sato K, Kogure T, Iwai H, Tanaka J (2002) J Am Ceram Soc 85:3054
74. Rey C, Collins B, Goehl T, Dickson IR, Glimcher MJ (1989) Calcif Tissue Int 45:157
75. Cowley JM, Moodie AF (1957) Acta Crystallogr 10:609
76. Henning PA, Landa-Cánovas AR, Larsson A-K, Lidin S (1999) Acta Crystallogr B 55:170
77. Nelson DGA, McLean JD, Sanders JV (1982) Radiat Eff Lett 68:51
78. Posner AS, Betts F (1975) Acc Chem Res 8:273
79. Onuma K, Ito A (1998) Chem Mater 10:3346